

Light Field-Based Underwater 3D Reconstruction Via Angular Resampling

Yuqi Ding¹ Zhang Chen^{1,3} Yu Ji² Jingyi Yu³ Jinwei Ye¹
¹Louisiana State University ² DGene U.S.A. ³ ShanghaiTech University

Abstract

Recovering 3D geometry of underwater scenes is challenging because of non-linear refraction of light at the water-air interface caused by the camera housing. We present a light field-based approach that leverages properties of angular samples for high-quality underwater 3D reconstruction from a single viewpoint. Specifically, we resample the light field image to angular patches. As underwater scenes exhibit weak view-dependent specularity, an angular patch tends to have uniform intensity when sampled at the correct depth. We thus impose this angular uniformity as a constraint for depth estimation. For efficient angular resampling, we design a fast approximation algorithm based on multivariate polynomial regression to approximate nonlinear refraction paths. We further develop a light field calibration algorithm that estimates the water-air interface geometry along with the camera parameters. Comprehensive experiments on synthetic and real data show our method produces state-of-the-art reconstruction on static and dynamic underwater scenes.

1. Introduction

3D Reconstruction of underwater scenes is of great interest and importance to many underwater exploration tasks, for example, robotic navigation [26, 44], seafloor mapping, [41, 45], and archaeological site preservation [21, 34, 66]. Affected by water as a participating medium, underwater 3D reconstruction faces challenges posed by scattering, absorption, and refraction. Nevertheless, the underwater environment also results in unique surface reflectance property that is beneficial to 3D reconstruction.

In this paper, we present a light field-based approach for high-quality underwater 3D reconstruction from a single viewpoint (see Fig. 1). We use refractive ray model to tackle the challenge posed by refraction. We consider the imaging setting that the camera is completely submerged in water by placing inside a watertight housing. The refraction thus happens on water-air interface at the lens port. We model non-linear light paths with one-time refraction for accurate depth estimation. Although there exist many solu-

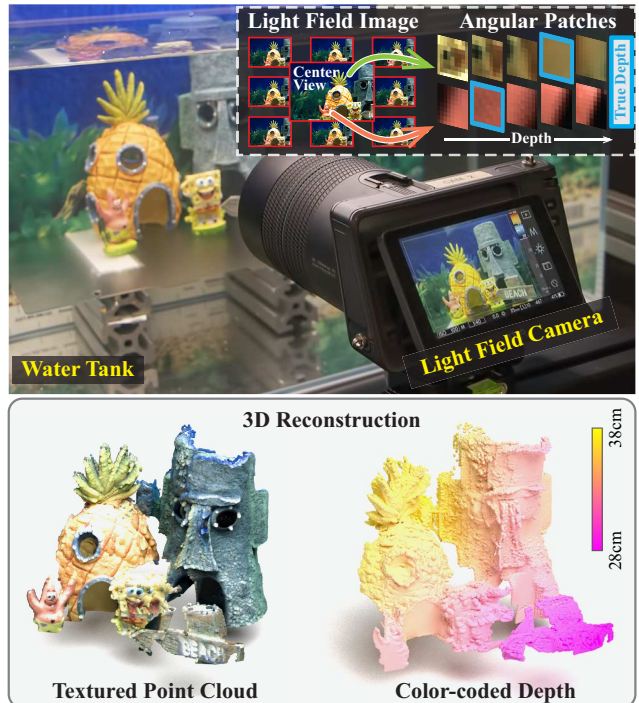


Figure 1. Light field-based 3D reconstruction via angular resampling. Top: Our experimental setup. We resample light field images to angular patches for depth estimation. Bottom: Our 3D reconstruction result in terms of point cloud. The point cloud is visualized with color texture (left) and color-coded depth (right).

tions that adapt multi-view stereo or structure-from-motion with refractive geometry [10, 11, 18, 23], our method differs in exploiting the benefit of angular ray samples. Besides, by using a light field camera, our method has the advantage of being a single-view solution.

A light field camera has a microlens array in between the imaging sensor and the main lens [43]. The microlenses spread out converging rays that come from the main lens, and thus allow the sensor to record angular samples from a scene point. Given scene point depths, we can resample light field images to angular patches, which are groups of rays that come from the same scene point. Note that the angular patches that we use here are not microlens images,

which in contrast collect angular samples from the same microlens. Similar angular sampling scheme is first proposed by Yu and McMillan [67] as surface light field. Because of refraction, it is non-trivial to resample these angular patches for underwater scenes. Even with closed-form ray tracing solutions, the computational cost is still very high because non-linear rays need to be traced for all sensor pixels at every depth candidate. We therefore design a fast approximation algorithm for efficient angular resampling. Specifically, we use a multivariate polynomial function to approximate the closed-form solution, which eliminates the need for per-pixel non-linear ray tracing.

The angular patches provide useful constraint for depth estimation. The key observation is that most objects exhibit much weaker view-dependent specular reflection in water than in air (see Fig. 5). Therefore, the angular patches should have uniform intensity when sampled at the correct depth. We call this property *angular uniformity*. With this constraint, we can estimate depth by minimizing the variance of angular patches. Although this weak-specular phenomenon of underwater reflectance is also described in several other literatures [14, 48, 53], its physical cause has not been rigorously examined. Here we provide a explanation for this phenomenon from the perspective of medium’s refractive index, by applying the Fresnel equations.

As we assume known camera parameters for angular patch resampling, we also develop a light field camera calibration algorithm that jointly estimates the camera intrinsics, extrinsics, and parameters relevant to the water-air interface (*i.e.*, the interface geometry and the refractive index of water). For validation, we perform extensive synthetic and real experiments. We also compare our method against off-the-self 3D scanners as well as state-of-the-art light field-based depth estimation algorithms. Results on static and dynamic scenes demonstrate that our method is highly accurate and robust for a variety of scenes.

2. Related Work

Underwater 3D Reconstruction. The problem of underwater 3D reconstruction has attracted much attention in the past decades. Many classical 3D reconstruction algorithms, including multi-view stereo [11, 12, 18, 36], structure-from-motion (SfM) [10, 23, 27, 50], structured light scanning [39, 40, 47], and photometric stereo [17, 38, 58] are adapted to the underwater setting either by considering the refractive geometry, or by compensating the absorption and scattering effect in water. Notably, Chari and Sturm [12] derive the multi-view geometry in refractive medium based on curved epipolar lines. Chadebecq *et al.* [10, 11] use multiple refractive planes to model relative camera motions, and solve SfM with refraction. Narasimhan *et al.* [40] take the scattering effect into account, and refine the structured light and photometric stereo methods for underwater scenes. Tsiot-

sios *et al.* [58] compensate the backscattering of point light sources in order to perform photometric stereo in murky water. Asano *et al.* [3, 4] leverage different absorption rate of near-infrared light for underwater depth estimation. The method is further extended as a one-shot solution for recovering dynamic scenes [37] and non-rigid scenes [29]. Several methods jointly recover the 3D of the water surface and the underwater scene with defocus cue [68], multi-view cue [46], and differentiable ray tracing [65].

As camera calibration is essential to 3D reconstruction, we also briefly review calibration methods developed for underwater settings. Lavest *et al.* [30] derive compensated lens models when using a camera underwater, and find that the magnifying effect of water refraction is equivalent to scaling the in-air focal length with the fluid’s refractive index. Treibitz *et al.* [56, 57] solve a simplified underwater calibration problem with a frontal-parallel refraction plane and known refractive index. Agrawal *et al.* [1] consider the problem of multiple refraction planes, and model underwater cameras with axial camera models. Haner *et al.* [20] study the extrinsic calibration in the presence of a single refraction. Chen and Yang [13] calibrate a stereo system in the presence of a thick flat refraction plane.

Light Field-Based Methods. Light field images record 4D spatial and angular samples of a scene. To capture a light field, one can either use a camera array [61, 64], or a compact light field camera with microlens array [43, 63]. Due to the multi-view nature, light field images are widely used for image synthesis and 3D reconstruction applications, including post-refocusing [33, 42, 60], novel view synthesis [9, 31, 32], and depth reconstruction [24, 54, 62]. A comprehensive evaluation of light field-based depth estimation methods can be found in [25]. Many algorithms have been developed for light field camera calibration by using different types of image features [6, 7, 15, 69].

Light field-based methods have also been developed for underwater applications. Some tackles the problems of low visibility and color distortions caused by scattering and absorption via jointly recovering clear underwater image and scene depth [52, 55, 59]. Skinner and Johnson-Roberson [51] develop a fast underwater 3D reconstruction solution using a light field camera. However, this method only accounts for the absorption of light in water without compensating for refraction. Ichimaru and Kawasaki [22] synthesize refraction-free images from light field and use them for stereo-based 3D reconstruction.

Our method uses a compact light field camera as imaging device and adopts refractive ray model for underwater 3D reconstruction. Different from existing methods, we exploit the angular uniformity of underwater scenes for depth estimation.

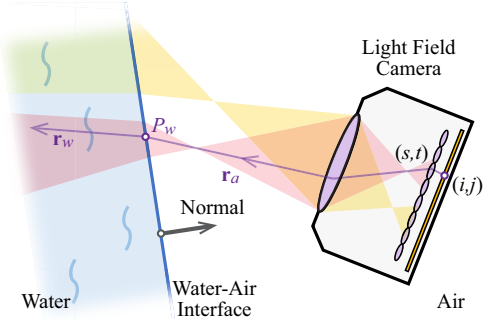


Figure 2. Underwater imaging setting. We assume that the ray is refracted once at the water-air interface.

3. Proposed Method

Here we present our light field-based method for underwater 3D reconstruction. We consider the one-time refraction on the water-air interface. We first introduce our calibration method under this setting (Sec. 3.1). We then describe our resampling scheme for forming the angular patches (Sec. 3.2). Lastly, we present our depth estimation algorithm (Sec. 3.3).

3.1. Light Field Camera Calibration

Our calibration algorithm aims at jointly estimating the interface parameters, which include the interface geometry and the refractive index of water, along with the camera parameters (including both intrinsics and extrinsics).

We consider the setting as shown in Fig. 2. The intrinsic parameters are used to map a pixel on the image plane to a ray that exits the light field camera. We represent a ray with a point on the ray and its direction. Assuming the main lens plane as $z = 0$, a ray exiting the camera can be represented by its main lens intersection point $P_a = (u, v, 0)^\top$, and direction $\mathbf{d}_a = (\sigma, \tau, 1)^\top$. A sub-aperture image pixel can be represented as a 4D coordinate $(s, t, i, j)^\top$, where (s, t) is the sub-aperture image index, and (i, j) is the pixel index within a sub-aperture image. Dansereau *et al.* [15] derive that the mapping between an image pixel and its exiting ray under the homogeneous coordinate can be expressed as a 5×5 matrix H with 12 non-zero elements:

$$\begin{bmatrix} u \\ v \\ \sigma \\ \tau \\ 1 \end{bmatrix} = \begin{bmatrix} H_1 & 0 & H_2 & 0 & H_3 \\ 0 & H_4 & 0 & H_5 & H_6 \\ H_7 & 0 & H_8 & 0 & H_9 \\ 0 & H_{10} & 0 & H_{11} & H_{12} \\ 0 & 0 & 0 & 0 & 1 \end{bmatrix} \begin{bmatrix} s \\ t \\ i \\ j \\ 1 \end{bmatrix}. \quad (1)$$

We further use the sixth-order polynomial distortion model [16] to compensate for lens distortions. We refer the non-zero elements in H : $\{H_1, \dots, H_{12}\}$ and the distortion parameters $\{k_1, k_2, k_3, b_1, b_2\}$ as the **intrinsic parameters** of a light field camera.

The in-air camera ray $\mathbf{r}_a : P_a + \lambda \mathbf{d}_a$ (where λ is the ray propagation factor) is refracted at the water-air interface. We then derive the origin and direction of the refracted ray. Assuming planar water-air interface, we have: $Ax + By + Cz + D = 0$. The point P_w where the camera ray enters the water is determined by λ_w :

$$\lambda_w = -\frac{Au + Bv + D}{A\sigma + B\tau + C}. \quad (2)$$

We use $P_w = P_a + \lambda_w \mathbf{d}_a$ as the origin of the refracted ray. By applying the Snell's law, the direction of the refracted ray can be calculated as:

$$\mathbf{d}_w = \frac{1}{n}(\mathbf{d}_a - (\alpha + \sqrt{n^2 - (1 - \alpha^2)})\mathbf{n}), \quad (3)$$

where \mathbf{d}_a is the camera ray's direction; $\mathbf{n} = (A, B, C)^\top / \sqrt{A^2 + B^2 + C^2}$ is the normal of water-air interface; $\alpha = \mathbf{n} \cdot \mathbf{d}_a$; and n is the refractive index of water (we assume the refractive index of air is 1). The refracted ray (or underwater ray) is then written as $\mathbf{r}_w : P_w + \lambda \mathbf{d}_w$.

We define the plane parameters $\{A, B, C, D\}$ and the refractive index of water n as the **interface parameters** as they determine the refractive medium.

We perform calibration with in-water checkerboard patterns. We use the **extrinsic parameters**: $\{R|T\}$ (where $R \in \mathbb{R}^{3 \times 3}$ is rotation matrix and $T \in \mathbb{R}^{3 \times 1}$ is translation vector) to transform a point P_m on the checkerboard to the camera coordinate: $P = RP_m + T$. As P should lie on the underwater ray \mathbf{r}_w , we minimize the point-to-ray distance between P and \mathbf{r}_w to solve the calibration parameters altogether (*i.e.*, intrinsics, interface, and extrinsics).

We consider the point-to-ray distance in two cases that are shown in Fig. 3. We first determine P is at which side of the interface plane. We compare the vector $\mathbf{l} = P - P_w$ with the plane normal \mathbf{n} . If \mathbf{l} and \mathbf{n} have opposite directions, P is on the water side; if they have the same direction, P is on the air side. Then, if P is on the water side (as it should be), we directly use its perpendicular distance from P to \mathbf{r}_w . If P is on the air side (which must be caused by incorrect parameter estimation), we use the length of \mathbf{l} as its distance to \mathbf{r}_w . In this way, we penalize the estimations that cause P to be on the wrong side of the interface plane. The point-to-ray distance $\varepsilon(P, \mathbf{r}_w)$ is therefore computed as:

$$\varepsilon(P, \mathbf{r}_w) = \begin{cases} \|\mathbf{l} - (\mathbf{l} \cdot \mathbf{d}_w)\mathbf{d}_w\|, & \mathbf{l} \cdot \mathbf{n} \leq 0, \\ \|\mathbf{l}\|, & \mathbf{l} \cdot \mathbf{n} > 0. \end{cases} \quad (4)$$

Suppose there are M feature points on the checkerboard, and we use N different pattern poses. We minimize the following objective function to solve for the calibration parameters:

$$\underset{\mathcal{I}, \mathcal{F}, \mathcal{E}}{\operatorname{argmin}} \sum_{\mathcal{I}}^N \sum_{\mathcal{E}}^M \varepsilon(RP_m + T, \mathbf{r}_w), \quad (5)$$

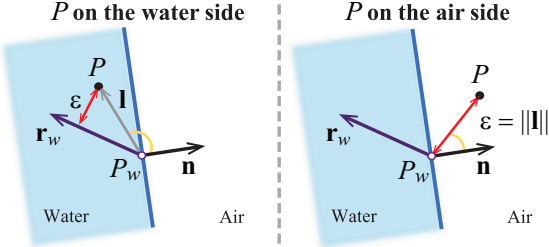


Figure 3. Two cases of the point-to-ray distance $\varepsilon(P, \mathbf{r}_w)$.

where $\mathcal{I} = \{H_{1,\dots,12}|k_{1,2,3}, b_{1,2}\}$ are intrinsic parameters; $\mathcal{F} = \{A, B, C, D|n\}$ are interface parameters; and $\mathcal{E} = \{R_{1,\dots,N}|T_{1,\dots,N}\}$ are extrinsic parameters. We use Levenberg-Marquardt algorithm to solve this optimization.

3.2. Angular Patch Resampling.

With the calibration parameters, we can resample the sub-aperture images to a bunch of angular patches, where each patch is a collection of rays that come from a same scene point. Fig. 4 (a) shows an example of angular patch. We formulate angular patches with respect to the center view image. The patch is formed by tracing rays back to each sub-aperture images given a scene depth d . Let $A^p(d)$ be an angular patch resampled at center view pixel p from a scene point P at depth d , and $\mathcal{H}^p : (s, t, d) \mapsto (i, j)$ be the mapping from a scene point at depth d to its projected pixel location (i, j) in sub-aperture image (s, t) . We can use \mathcal{H}^p to locate pixels in sub-aperture images that form $A^p(d)$.

Due to refraction, the calculation of \mathcal{H} is non-trivial. We first show that a closed-form solution can be derived by applying the Snell's law. However, the closed-form solution is a complex equation that needs to be solved at all pixels for all depth labels, which is computationally expensive. We then design an approximation method based on multivariate polynomial regression.

We first derive the closed-form solution to this ray tracing problem. As shown in Fig. 4 (b), given a pixel p in the center view, we can trace out an underwater ray from its center of projection (CoP) P_a^c . Given depth d , we can sample a scene point P along this ray. Let P_a be the CoP of another sub-aperture image. P' , P'_a are the projected points of P , P_a on the water-air interface. \mathbf{r}_a and \mathbf{r}_w are the refracted ray segments that project P to the sub-aperture image at P_a . P_w is the intersection point where refraction happens. To obtain the projected pixel (i, j) of P , we need to solve for P_w .

To simplify notations, we denote $\gamma = \|P'_a - P_w\|$ and $\kappa = \|P' - P\|$. By applying the Snell's law, we have

$$\gamma^2((\kappa - \gamma)^2 + \|P' - P\|^2) - n^2(\kappa - \gamma)^2(\gamma^2 + \|P'_a - P_a\|^2) = 0. \quad (6)$$

Given P and P_a , Eq. (6) is a univariate fourth-order equation of γ and has up to four real solutions. The so-

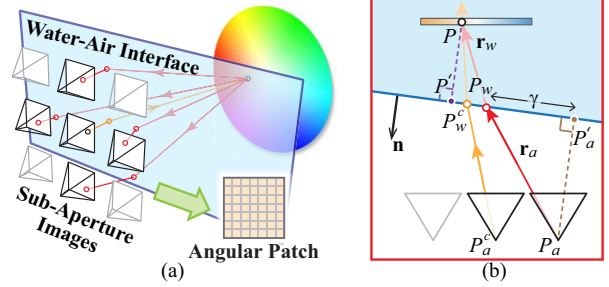


Figure 4. (a) The angular patch is a collection of rays that come from the same scene point. (b) Sampling an angular ray in sub-aperture image.

lutions can be computed via closed-form formulas [49]. As shown in [19], only one solution is valid. With γ , we have $P_w = P'_a + \gamma(P' - P'_a)$. With $\mathbf{r}_a = P_w - P_a$, we can locate the projected pixel (i, j) with intrinsic parameters.

In our approximation method, we establish a mapping between (s, t, d) and γ without solving Eq. (6) for all sub-aperture views and depth candidates. Given a pixel p in the center view, we denote such mapping as $\mathcal{G}^p : (s, t, d) \mapsto \gamma$. As microlens-based light field camera has small baseline, we experimentally observe that \mathcal{G}^p can be approximated by a multivariate cubic polynomial function $\tilde{\mathcal{G}}^p(s, t, d)$.

At each center view pixel p , we compute 64 uniform samples of γ with respect to (s, t, d) in a $4 \times 4 \times 4$ grid. With these pairs of (s, t, d) and γ , we solve the polynomial coefficients of $\tilde{\mathcal{G}}^p$ via least squares regression. The resulting $\tilde{\mathcal{G}}^p$ is then used to calculate γ at each (s, t) and depth candidate d . Compared with the closed-form solution, our approximation method is able to achieve $10\times$ speedup.

We test on a light field with spatial resolution 625×434 and angular resolution 11×11 , and 100 depth candidates per pixel. When implemented with Matlab without GPU acceleration, the closed-form solution takes over 20 min to compute all angular patches, as fourth-order equation needs to be solved for $625 \times 434 \times 11 \times 11 \times 100$ times. In contrast, our approximation method only takes 2 min to resample all the patches. The average error of γ computed with our approximation method is $0.01mm$.

Uniformity of Angular Patch. We find that the angular patches tend to have uniform intensity for underwater scenes. This is because underwater surface reflectance has weak view-dependent specular reflection. We show a comparison between the underwater and in-air reflectance of the same object in Fig. 5. By applying the Fresnel equations, we show that this phenomenon is due to the low gradient of refractive index between water and common materials in real-world objects (*e.g.*, plastic, ceramic, *etc.*).

The Fresnel equations give us the reflection rate of light when incident on the interface between two media:

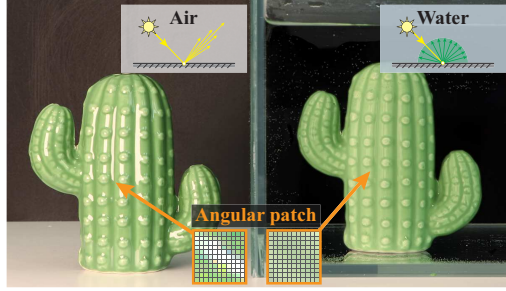


Figure 5. Underwater scenes exhibit very weak specular reflection that results in the uniformity of angular patch. We show pictures of the same object captured in air (left) vs. underwater (right).

$$\eta = \frac{1}{2} \left(\left| \frac{n_1 k_1 - n_2 k_2}{n_1 k_1 + n_2 k_2} \right|^2 + \left| \frac{n_1 k_2 - n_2 k_1}{n_1 k_2 + n_2 k_1} \right|^2 \right), \quad (7)$$

where n_1 and n_2 are the media's refractive indices (light travels from n_1 to n_2); θ_i is the incident angle; $k_1 = \cos \theta_i$; and $k_2 = \cos \sqrt{1 - (n_2 - n_1 \sin \theta_i) / n_2}$.

This equation shows that when the two media have similar refractive indices (i.e., $n_1 \approx n_2$), the η value is likely to be small, which indicates that light will be mostly transmitted (which causes diffuse reflection), instead of being directly reflected (which causes specular reflection). As water is a dense medium, its refractive index (i.e., 1.33) is closer to common materials (e.g., plastics 1.3 \sim 1.7, porcelain \sim 1.5) than air. These objects thus exhibit much weaker specular reflection in water than in air. This phenomenon has exception for metal surfaces, whose refractive indices are complex numbers. Direct reflection therefore still largely exists on metal surfaces. Please see our supplementary material for comparison between underwater and in-air reflection rates for various materials.

This weak specular phenomenon results in the uniformity of angular patches that is useful for depth estimation.

3.3. Depth Estimation

The scene depth is estimated by solving an optimization with two constraints: 1) uniformity of angular patches, and 2) color and gradient consistency along curved epipolar lines. Note that the two constraints appear to be the same when the true depths are known, but the costs are computed in different ways. The two constraints are thus complementary.

Angular Uniformity Constraint. In Sec. 3.2, we show that the angular patches have uniform intensity when sampled at correct depth because of the weak specular phenomenon. Angular ray samples traced from the wrong depth might have different colors as they in fact come from different scene points. Therefore, we use the color variance of angular patches as constraint for depth estimation. We plot the variances of an angular patch with respect to the depth

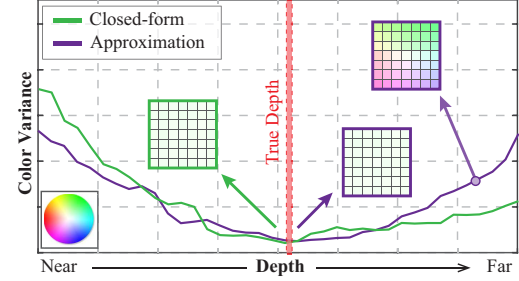


Figure 6. Angular patch variance with respect to depth.

in Fig. 6. We compare the curve computed with our approximation algorithm against the closed-form solution. We can see the two curves are close. In both plots, the variance is lowest when sampled at the true depth. Wrong depths result in non-uniform angular patch and thus large variance. The cost function of the angular uniformity constraint is written as:

$$E_{angular}(p, d) = \frac{1}{ST-1} \sum_{t=1}^T \sum_{s=1}^S |A_{s,t}^p(d) - \mu|^2, \quad (8)$$

where $A^p(d)$ is the angular patch for a pixel p in the center view, sampled at depth d ; (s, t) is sub-aperture image index; (S, T) is the angular resolution; and μ is the mean of $A^p(d)$.

Color and Gradient Consistency. We also adopt the color and gradient consistency along epipolar lines as constraint for depth estimation. For underwater scenes, the epipolar lines are curved due to refraction [12]. The epipolar curves in sub-aperture images can be formed with the angular rays. We compare the color and color gradient of pixels along the epipolar curves with corresponding center view pixel. Let $f_{s,t}^p$ be the epipolar curve for center view pixel p in sub-aperture image (s, t) . Our cost functions are written as:

$$E_{color}(p, d) = \sum_{t=1}^T \sum_{s=1}^S |I_c(p) - I_{s,t}(f_{s,t}^p(d))|, \quad (9)$$

$$E_{grad}(p, d) = \sum_{t=1}^T \sum_{s=1}^S |G_c(p) - G_{s,t}(f_{s,t}^p(d))|, \quad (10)$$

where I is intensity image (I_c refers to the center view); G is the combined gradient of intensity image I (i.e., $G = \partial I / \partial x + \partial I / \partial y$).

Optimization. Our final objective function combines Eqs. (8), (9), (10) and an additional smoothness term:

$$\operatorname{argmin}_d \sum_p (\beta_1 E_{color} + \beta_2 E_{grad} + \beta_3 E_{angular} + \beta_4 E_{smooth}) \quad (11)$$

where $\beta_{1,...,4}$ are weights for balancing the four terms; $E_{smooth} = \sum_{p_N} \|d(p) - d(p_N)\|$ is the smoothness term that enforces depth smoothness, where p_N is the set of neighboring pixels around p . The optimization is solved with multi-label graph cut [28].

4. Experiments

4.1. Synthetic Experiments

We simulate light field images of underwater scenes through ray tracing. The synthesized light fields have 11×11 sub-aperture images with spatial resolution 625×434 . The equivalent baseline is $b = 0.4\text{mm}$.

We set the refractive index of air to 1, and use three different sets of interface parameters: $\mathcal{F}_1 = \{0, 0, -1, 0.1|1.333\}$, $\mathcal{F}_2 = \{0, 0, -1, 0.1|1.45\}$, and $\mathcal{F}_3 = \{0.1476, 0.0984, -0.9841, 0.1|1.333\}$. \mathcal{F}_1 and \mathcal{F}_2 are frontal-parallel interface planes, but with different refractive indices of water. \mathcal{F}_3 is an oblique interface plane.

Underwater Calibration. We simulate a 6×7 checkerboard in water, and randomly generate different poses.

For intrinsic parameters, we compare with three state-of-the-art methods: 1) **SV** [8]: a classical calibration method for conventional camera at a single viewpoint; 2) **TB** [15]: the calibration algorithm from the Light Field Toolbox for Matlab; and 3) **MPC** [69]: a recent light field camera calibration method that uses a multi-projection-center model to reduce the parameter space. All these methods are designed for in-air calibration without considering refraction. For **SV** [8], we use the center view image as input.

Table 1 shows the intrinsic calibration results under the interface setting \mathcal{F}_3 . See additional results for \mathcal{F}_1 and \mathcal{F}_2 in the supplementary material. We can see that the estimated baselines of all methods (except **SV** [8]) are not affected much by refraction. However, the estimated focal lengths from all air-based methods are closer to the ground truth multiplied by the refractive index ($550 \times 1.333 = 733.15$). In contrast, our method separates refraction and is able to estimate more accurate intrinsic parameters.

	SV	TB	MPC	Ours	GT
b	-	4.2716e-4	4.1310e-4	4.0003e-4	4.00e-4
f_x	789.2850	776.4190	787.9620	550.5019	550
f_y	789.8730	766.5866	788.5638	550.5043	550
c_x	354.9465	312.5197	354.2245	313	312.5
c_y	249.9410	217.5023	249.5642	217.5	217

Table 1. Estimated intrinsic parameters under interface setting \mathcal{F}_3 .

As our method also calibrates the interface parameters \mathcal{F} (which includes the plane coefficient and the refractive index of water), we show our calibration results under the three interface settings in comparison with the ground truths in Table 2. We can see that our estimations are accurate under various interface orientations and refractive indices.

For extrinsic parameters, we add two other methods that assume known intrinsics for comparison: 1) **SVA**: the classical calibration method [8] that uses the ground truth intrin-

	\mathcal{F}_1		\mathcal{F}_2		\mathcal{F}_3	
	GT	Ours	GT	Ours	GT	Ours
A	0	-0.0014	0	-0.0014	0.1476	0.1470
B	0	-0.0018	0	-0.0011	0.0984	0.0975
C	-1	-1	-1	-1	-0.9841	-0.9843
D	0.1	0.1001	0.1	0.1001	0.1	0.1005
n	1.333	1.3364	1.45	1.4601	1.333	1.3384

Table 2. Estimated interface parameters under all three settings.

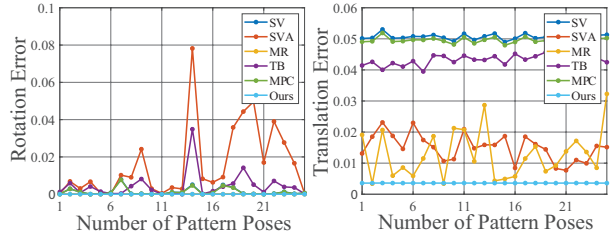


Figure 7. Extrinsic estimation errors under interface setting \mathcal{F}_3 .

sic parameters in air; and 2) **MR** [1]: the multi-refractive layer underwater calibration method that uses the ground truth intrinsic and interface parameters. For each method, we evaluate the estimated rotation and translation with respect to different numbers of pattern poses. Fig. 7 shows the estimation errors of extrinsics under the interface setting \mathcal{F}_3 . See the supplementary material for errors under the other two interface settings, and the visualization of extrinsic calibration results.

Depth Estimation. Given the calibration parameters, we evaluate our depth estimation algorithm. In this experiment, we use the interface parameter $\mathcal{F}_1 = \{0, 0, -1, 0.1|1.333\}$, and test on a planar target. We compare with a state-of-the-art light field based depth estimation method [24]. For fair comparison, we first use their algorithm to estimate a disparity map, and then use the ground truth intrinsics and interface parameters to convert disparities into depth values. Fig. 8 compares the reconstruction results. Our result is very close to the ground truth plane. In contrast, the result of [24] appears to be curved because it uses straight epipolar lines that don't account for refraction.

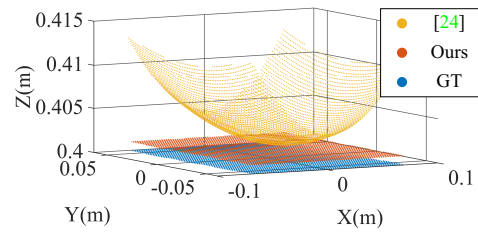


Figure 8. Synthetic 3D reconstruction results of a plane.



Figure 9. Quantitative evaluation on three depth layers. From left to right: acquisition setup, center view of the captured light field, and our estimated depth map.

4.2. Real Experiments

We use a Lytro Illum camera to capture underwater scenes submerged in a water tank of size $60cm \times 30cm \times 36cm$. Our experimental setup is shown in Fig. 1. The captured light field image has a total resolution of 7728×5368 . We decode it to 15×15 sub-aperture images (*i.e.*, angular resolution), each with spatial resolution 625×434 . See the supplementary material for our camera calibration results.

Ablation Study. As shown in Fig. 9, we quantitatively evaluate our method using underwater planar boards at three different depths ($9cm$, $15cm$, $20cm$). The ground truth depths are measured with a ruler. Table 3 shows the depth estimation errors (in mm) for the three planar boards, as well as the ablation study on the terms in our objective function (Eq. (11)). We can see that our proposed angular uniformity constraint ($E_{angular}$) effectively improves the reconstruction accuracy.

	Plane 1	Plane 2	Plane 3
w/o $E_{angular}$, E_{smooth}	2.8587	7.7169	10.9305
w/o $E_{angular}$	1.9112	6.5741	7.8348
w/o E_{smooth}	1.8294	2.3673	3.2337
Ours (all terms included)	1.7852	1.1930	2.4445

Table 3. Ablation study on the terms in our objective function. The unit of depth estimation error is mm .

Static Scene Reconstruction. We first use one light field camera to capture various static underwater scenes. We compare our method with structured light (**SL**), time-of-flight (**ToF**), and a light field based depth estimation method from [24]. Note that **SL** and **ToF** are active 3D reconstruction methods. For **SL**, we build a projector-camera system for 3D scanning. In the system, we use a 1280×720 laser projector and a 2448×2048 monochrome camera. Both projector and camera are calibrated with underwater patterns [35]. We use the Gray code patterns, and recover the point cloud by ray triangulation without considering refraction. For **ToF**, we use the Azure Kinect to scan the underwater scenes and recover its point cloud using the default

SDK. We also implement a **ToF** variant that compensates the reconstruction results with the refractive index of water, which is denoted as **ToF***. For [24], we combine it with the calibration result from our method so that the conversion from disparity to depth correctly accounts for refraction.

To obtain ground truth, we use structured light method to scan the objects in air. Table 4 compares the Root Mean Squared Error (RMSE) of reconstructed point clouds using different methods for five scenes. The qualitative results for the “Vase” and “Skull” scenes are shown in Fig. 10. Other qualitative results are included in the supplementary material. For underwater **SL**, the recovered point clouds are noisy and distorted because the rays cannot be properly triangulated when refraction is not considered. **ToF** results suffer from large errors because the velocity of light is smaller in water than in air. Although **ToF*** greatly improves over **ToF**, its accuracy is still lower than our method. [24] assumes linear epipolar lines. Thus its disparity computation does not take refraction into account. As a result, its results are less accurate than our method.

Method	SL	ToF	ToF*	Our Calib. + [24]	Ours
Vase	8.457	23.377	8.433	4.240	2.161
Skull	6.509	25.526	8.433	12.754	3.572
Board	6.036	25.082	8.490	3.021	2.899
House	3.505	17.067	6.687	4.064	2.374
Turtle	3.418	14.880	12.326	4.247	2.692

Table 4. RMSE comparison (in mm) of 3D reconstruction results.

We also perform experiments with two light field cameras. The two cameras are placed side by side in order to have large overlap in the field of view. We perform 3D reconstruction on each light field and show that the point clouds reconstructed by our method can be naturally aligned without using any fitting algorithms (*e.g.*, ICP [5]). For comparison, we combine two light field camera calibration algorithms (**TB** [15] and **MPC** [69]) with the light field depth estimation method [24]. We perform **TB** with in-air calibration targets, while **MPC** with underwater ones. We also combine [24] with our calibration results. Note that **TB** and **MPC** cannot calibrate interface parameters, so **TB** + [24] and **MPC** + [24] do not take refraction into account. The point cloud fusion results are shown in Fig. 11. We can see that all the comparison methods exhibit clear misalignments in their fusion results. In contrast, our point clouds are well aligned without explicit fitting.

Dynamic Scene Reconstruction. Finally, we perform experiments to recover a dynamic underwater scene. Our dynamic scene consists of a goldfish swimming in front of an aquarium castle (see Fig. 12). Here we choose to use a small aquarium of size $30cm \times 30cm \times 30cm$, because the field of

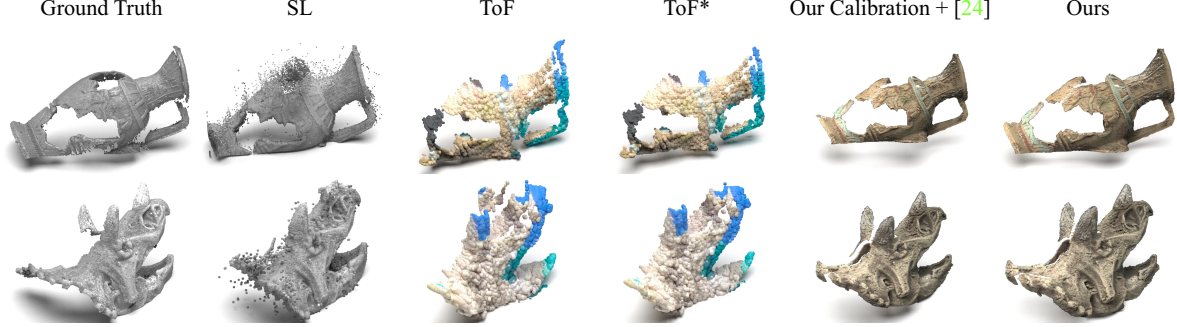


Figure 10. 3D reconstruction results with one light field camera in comparison with state-of-the-arts.

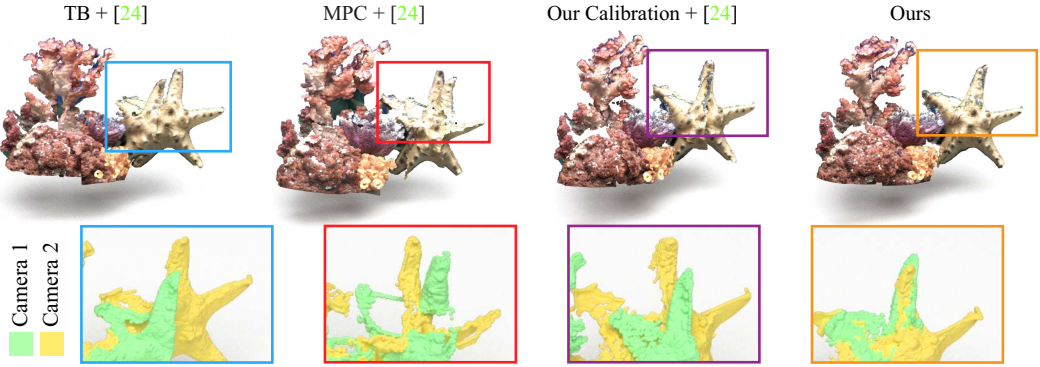


Figure 11. Point cloud fusion results with two light field cameras. We directly fuse the point clouds without applying fitting algorithms. The second row shows zoom-in views that display the two point clouds in different colors.

view and focus range of the camera are small. We use one Lytro camera to capture a video at 10 frames per second. As Lytro doesn't have video mode, we implement continuous triggering function with an external control board. We first calibrate the camera, and then perform 3D reconstruction on each frame of the recorded video. We show three consecutive frames of the reconstruction results in Fig. 12. Our method can well recover the fine structures of the goldfish, such as the fin and the tail. But notice that the colors of the fin and tail are dark in some frames, as they are semi-transparent and blend in the black background color. Although our frame rate is low (10 fps), the reconstruction results still illustrate the fish's motion trajectory well. This shows that our method can be used for 3D video acquisition.

5. Conclusions & Discussions

In this paper, we present a light field-based method for underwater 3D reconstruction from a single viewpoint. We demonstrated using the angular uniformity for depth estimation. We designed an approximation method to address the efficiency of angular patch calculation. We also developed a calibration algorithm that jointly estimates the camera parameters with the interface attributes. Our method is validated with extensive experiments.

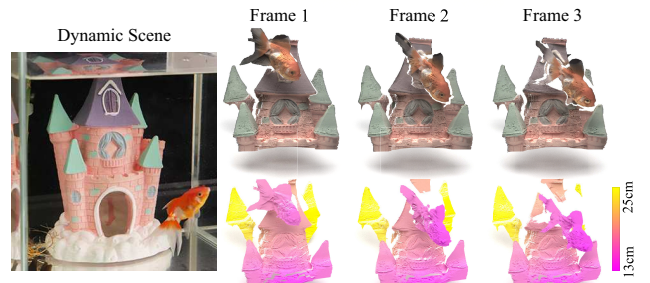


Figure 12. Dynamic scene reconstruction. Left: Scene setup. Right: 3D reconstruction results at three time frames. We visualize the point clouds in color texture (Row One) and color-coded depths (Row Two).

One limitation of our method is that the scattering and attenuation effects are not being considered. To alleviate the problem, we can preprocess underwater images with color restoration algorithms (e.g., [2]) for better visibility. Due to the small baseline of light field camera, our method only works well for close-range, small-scale scenes. Camera arrays need to be used for recovering large-scale scenes. In the future, we plan to build more versatile imaging systems to overcome the challenges of underwater imaging.

References

[1] Amit Agrawal, Srikanth Ramalingam, Yuichi Taguchi, and Visesh Chari. A theory of multi-layer flat refractive geometry. In *IEEE Conference on Computer Vision and Pattern Recognition (CVPR)*, 2012. 2, 6

[2] Derya Akkaynak and Tali Treibitz. Sea-thru: A method for removing water from underwater images. In *IEEE/CVF Conference on Computer Vision and Pattern Recognition (CVPR)*, 2019. 8

[3] Yuta Asano, Yinqiang Zheng, Ko Nishino, and Imari Sato. Shape from water: Bispectral light absorption for depth recovery. In *European Conference on Computer Vision (ECCV)*, 2016. 2

[4] Yuta Asano, Yinqiang Zheng, Ko Nishino, and Imari Sato. Depth sensing by near-infrared light absorption in water. *IEEE Transactions on Pattern Analysis and Machine Intelligence*, 43(8):2611–2622, 2021. 2

[5] Paul J. Besl and Neil D. McKay. A method for registration of 3-D shapes. *IEEE Transactions on Pattern Analysis and Machine Intelligence*, 14(2):239–256, 1992. 7

[6] Yunsu Bok, Hae-Gon Jeon, and In So Kweon. Geometric calibration of micro-lens-based light-field cameras using line features. In *European Conference on Computer Vision (ECCV)*, 2014. 2

[7] Yunsu Bok, Hae-Gon Jeon, and In So Kweon. Geometric calibration of micro-lens-based light field cameras using line features. *IEEE Transactions on Pattern Analysis and Machine Intelligence*, 39(2):287–300, 2016. 2

[8] Jean-Yves Bouguet. Camera calibration toolbox for matlab, http://www.vision.caltech.edu/bouguetj/calib_doc/index.html. 6

[9] Chris Buehler, Michael Bosse, Leonard McMillan, Steven Gortler, and Michael Cohen. Unstructured lumigraph rendering. In *28th Annual Conference on Computer Graphics and Interactive Techniques*, 2001. 2

[10] François Chadebecq, Francisco Vasconcelos, George Dwyer, René Lacher, Sébastien Ourselin, Tom Vercauteren, and Danail Stoyanov. Refractive structure-from-motion through a flat refractive interface. In *IEEE International Conference Computer Vision (ICCV)*, 2017. 1, 2

[11] François Chadebecq, Francisco Vasconcelos, René Lacher, Efthymios Maneas, Adrien Desjardins, Sébastien Ourselin, Tom Vercauteren, and Danail Stoyanov. Refractive two-view reconstruction for underwater 3D vision. *International Journal of Computer Vision*, pages 1101–1117, 2019. 1, 2

[12] Visesh Chari and Peter Sturm. Multiple-view geometry of the refractive plane. In *British Machine Vision Conference (BMVC)*, 2009. 2, 5

[13] Xida Chen and Yee-Hong Yang. Two-view camera housing parameters calibration for multi-layer flat refractive interface. In *IEEE Conference on Computer Vision and Pattern Recognition (CVPR)*, 2014. 2

[14] Thomas W. Cronin, Nadav Shashar, Roy L. Caldwell, Justin Marshall, Alexander G. Cheroske, and Tsyr-Huei Chiou. Polarization vision and its role in biological signaling. *Integrative and Comparative Biology*, 43(4):549–558, 2003. 2

[15] Donald G. Dansereau, Oscar Pizarro, and Stefan B. Williams. Decoding, calibration and rectification for lenslet-based plenoptic cameras. In *IEEE Conference on Computer Vision and Pattern Recognition (CVPR)*, 2013. 2, 3, 6, 7

[16] Brown C. Duane. Close-range camera calibration. *Photogrammetric Engineering*, 37(8):855–866, 1971. 3

[17] Yuki Fujimura, Masaaki Iiyama, Atsushi Hashimoto, and Michihiko Minoh. Photometric stereo in participating media considering shape-dependent forward scatter. In *IEEE Conference on Computer Vision and Pattern Recognition (CVPR)*, 2018. 2

[18] Jason Gedge, Minglun Gong, and Yee-Hong Yang. Refractive epipolar geometry for underwater stereo matching. In *Canadian Conference on Computer and Robot Vision*, 2011. 1, 2

[19] Georg Glaeser and Hans-Peter Schröcker. Reflections on refractions. *Journal for Geometry and Graphics*, 4(1):1–18, 2000. 4

[20] Sebastian Haner and Kalle Åström. Absolute pose for cameras under flat refractive interfaces. In *IEEE Conference on Computer Vision and Pattern Recognition (CVPR)*, 2015. 2

[21] Jon Henderson, Oscar Pizarro, Matthew Johnson-Roberson, and Ian Mahon. Mapping submerged archaeological sites using stereo-vision photogrammetry. *International Journal of Nautical Archaeology*, 42(2):243–256, 2013. 1

[22] Kazuto Ichimaru and Hiroshi Kawasaki. Underwater stereo using refraction-free image synthesized from light field camera. In *IEEE International Conference of Image Processing (ICIP)*, 2019. 2

[23] Kazuto Ichimaru, Yuichi Taguchi, and Hiroshi Kawasaki. Unified underwater structure-from-motion. In *IEEE International Conference on 3D Vision (3DV)*, 2019. 1, 2

[24] Hae-Gon Jeon, Jaesik Park, Gyeongmin Choe, Jinsun Park, Yunsu Bok, Yu-Wing Tai, and In So Kweon. Accurate depth map estimation from a lenslet light field camera. In *IEEE Conference on Computer Vision and Pattern Recognition (CVPR)*, 2015. 2, 6, 7

[25] Ole Johannsen, Katrin Honauer, Bastian Goldluecke, Anna Alperovich, Federica Battisti, Yunsu Bok, Michele Brizzi, Marco Carli, Gyeongmin Choe, Maximilian Diebold, et al. A taxonomy and evaluation of dense light field depth estimation algorithms. In *IEEE Conference on Computer Vision and Pattern Recognition Workshop (CVPRW)*, 2017. 2

[26] Matthew Johnson-Roberson, Oscar Pizarro, Stefan B Williams, and Ian Mahon. Generation and visualization of large-scale three-dimensional reconstructions from underwater robotic surveys. *Journal of Field Robotics*, 27(1):21–51, 2010. 1

[27] Anne Jordt-Sedlazeck and Reinhard Koch. Refractive structure-from-motion on underwater images. In *IEEE International Conference Computer Vision (ICCV)*, 2013. 2

[28] Vladimir Kolmogorov and Ramin Zabih. Multi-camera scene reconstruction via graph cuts. In *European Conference on Computer Vision (ECCV)*, 2002. 5

[29] Meng-Yu Jennifer Kuo, Ryo Kawahara, Shohei Nobuhara, and Ko Nishino. Non-rigid shape from water. *IEEE*

Transactions on Pattern Analysis and Machine Intelligence, 43(7):2220–2232, 2021. 2

[30] Jean-Marc Lavest, Gérard Rives, and Jean-Thierry Lapresté. Underwater camera calibration. In *European Conference on Computer Vision (ECCV)*. 2

[31] Marc Levoy and Pat Hanrahan. Light field rendering. In *23rd Annual Conference on Computer Graphics and Interactive Techniques*, 1996. 2

[32] Zhouchen Lin and Heung-Yeung Shum. A geometric analysis of light field rendering. *International Journal of Computer Vision*, pages 121–138, 2004. 2

[33] Andrew Lumsdaine and Todor Georgiev. The focused plenoptic camera. In *IEEE International Conference on Computational Photography*, 2009. 2

[34] John McCarthy. Multi-image photogrammetry as a practical tool for cultural heritage survey and community engagement. *Journal of Archaeological Science*, 43:175–185, 2014. 1

[35] Daniel Moreno and Gabriel Taubin. Simple, accurate, and robust projector-camera calibration. In *Second International Conference on 3D Imaging, Modeling, Processing, Visualization Transmission*, 2012. 7

[36] Nigel J.W. Morris and Kiriakos N. Kutulakos. Dynamic refraction stereo. In *IEEE International Conference Computer Vision (ICCV)*, 2005. 2

[37] Satoshi Murai, Meng-Yu Kuo, Ryo Kawahara, Shohei Nobuhara, and Ko Nishino. Surface normals and shape from water. In *IEEE/CVF International Conference Computer Vision (ICCV)*, 2019. 2

[38] Zak Murez, Tali Treibitz, Ravi Ramamoorthi, and David J. Kriegman. Photometric stereo in a scattering medium. *IEEE Transactions on Pattern Analysis and Machine Intelligence*, 39(9):1880–1891, 2017. 2

[39] Srinivasa G. Narasimhan and Shree K. Nayar. Structured light methods for underwater imaging: light stripe scanning and photometric stereo. In *Proceedings of the MTS/IEEE Oceans*, pages 2610–2617, 2005. 2

[40] Srinivasa G. Narasimhan, Shree K. Nayar, Bo Sun, and Sanjeev J. Koppal. Structured light in scattering media. In *IEEE International Conference Computer Vision (ICCV)*, 2005. 2

[41] Shahriar Negahdaripour and Hossein Madjidi. Stereovision imaging on submersible platforms for 3-D mapping of benthic habitats and sea-floor structures. *IEEE Journal of Oceanic Engineering*, 28(4):625–650, 2003. 1

[42] Ren Ng. Fourier slice photography. In *ACM SIGGRAPH*, pages 735–744. 2005. 2

[43] Ren Ng, Marc Levoy, Mathieu Brédif, Gene Duval, Mark Horowitz, Pat Hanrahan, et al. Light field photography with a hand-held plenoptic camera. *Computer Science Technical Report (CSTR)*, 2(11):1–11, 2005. 1, 2

[44] Liam Paull, Sajad Saeedi, Mae Seto, and Howard Li. Auv navigation and localization: A review. *IEEE Journal of Oceanic Engineering*, 39(1):131–149, 2013. 1

[45] Oscar Pizarro, Ryan Michael Eustice, and Hanumant Singh. Large area 3-D reconstructions from underwater optical surveys. *IEEE Journal of Oceanic Engineering*, 34(2):150–169, 2009. 1

[46] Yiming Qian, Yinqiang Zheng, Minglun Gong, and Yee-Hong Yang. Simultaneous 3D reconstruction for water surface and underwater scene. In *European Conference on Computer Vision (ECCV)*, 2018. 2

[47] Amin Sarafraz and Brian K. Haus. A structured light method for underwater surface reconstruction. *ISPRS Journal of Photogrammetry and Remote Sensing*, 114:40–52, 2016. 2

[48] Yoav Y. Schechner and Nir Karpel. Recovery of underwater visibility and structure by polarization analysis. *IEEE Journal of Oceanic Engineering*, pages 570–587, 2005. 2

[49] Jochen Schwarze. Cubic and quartic roots. In *Graphics Gems*, pages 404–407. 1990. 4

[50] Anne Sedlazeck and Reinhard Koch. Calibration of housing parameters for underwater stereo-camera rigs. In *British Machine Vision Conference (BMVC)*, 2011. 2

[51] Katherine A. Skinner and Matthew Johnson-Roberson. Towards real-time underwater 3D reconstruction with plenoptic cameras. In *IEEE/RSJ International Conference on Intelligent Robots and Systems (IROS)*, 2016. 2

[52] Katherine A. Skinner and Matthew Johnson-Roberson. Underwater image dehazing with a light field camera. In *IEEE Conference on Computer Vision and Pattern Recognition Workshop (CVPRW)*, 2017. 2

[53] Yohay Swirski, Yoav Y. Schechner, Ben Herzberg, and Shahriar Negahdaripour. Caustereo: Range from light in nature. *Applied Optics*, 50(28):89–101, Oct 2011. 2

[54] Michael W Tao, Sunil Hadap, Jitendra Malik, and Ravi Ramamoorthi. Depth from combining defocus and correspondence using light-field cameras. In *IEEE International Conference Computer Vision (ICCV)*, 2013. 2

[55] Jiandong Tian, Zak Murez, Tong Cui, Zhen Zhang, David Kriegman, and Ravi Ramamoorthi. Depth and image restoration from light field in a scattering medium. In *IEEE International Conference Computer Vision (ICCV)*, 2017. 2

[56] Tali Treibitz, Yoav Y. Schechner, Clayton Kunz, and Hanumant Singh. Flat refractive geometry. *IEEE Transactions on Pattern Analysis and Machine Intelligence*, 34(1):51–65, 2011. 2

[57] Tali Treibitz, Yoav Y. Schechner, and Hanumant Singh. Flat refractive geometry. In *IEEE Conference on Computer Vision and Pattern Recognition (CVPR)*, 2008. 2

[58] Chourmouzios Tsotsios, Maria E. Angelopoulou, Tae-Kyun Kim, and Andrew J. Davison. Backscatter compensated photometric stereo with 3 sources. In *IEEE Conference on Computer Vision and Pattern Recognition (CVPR)*, 2014. 2

[59] Vigil Varghese, Mitch Bryson, Oscar Pizarro, Stefan B. Williams, and Donald G. Dansereau. Light field image restoration for vision in scattering media. In *IEEE International Conference of Image Processing (ICIP)*, 2018. 2

[60] Ashok Veeraraghavan, Ramesh Raskar, Amit Agrawal, Ankit Mohan, and Jack Tumblin. Dappled photography: Mask enhanced cameras for heterodyned light fields and coded aperture refocusing. *ACM Transaction on Graphics*, 26(3):69, 2007. 2

[61] Kartik Venkataraman, Dan Lelescu, Jacques Duparré, Andrew McMahon, Gabriel Molina, Priyam Chatterjee, Robert

Mullis, and Shree Nayar. Picam: An ultra-thin high performance monolithic camera array. *ACM Transaction on Graphics*, 32(6):1–13, 2013. 2

[62] Ting-Chun Wang, Alexei A Efros, and Ravi Ramamoorthi. Occlusion-aware depth estimation using light-field cameras. In *IEEE International Conference Computer Vision (ICCV)*, 2015. 2

[63] Li-Yi Wei, Chia-Kai Liang, Graham Myhre, Colvin Pitts, and Kurt Akeley. Improving light field camera sample design with irregularity and aberration. *ACM Transaction on Graphics*, 34(4):1–11, 2015. 2

[64] Bennett Wilburn, Neel Joshi, Vaibhav Vaish, Eino-Ville Talvala, Emilio Antunez, Adam Barth, Andrew Adams, Mark Horowitz, and Marc Levoy. High performance imaging using large camera arrays. In *ACM SIGGRAPH*. 2005. 2

[65] Jinhui Xiong and Wolfgang Heidrich. In-the-wild single camera 3D reconstruction through moving water surfaces. In *IEEE/CVF International Conference Computer Vision (ICCV)*, 2021. 2

[66] Kotaro Yamafune, Rodrigo Torres, and Filipe Castro. Multi-image photogrammetry to record and reconstruct underwater shipwreck sites. *Journal of Archaeological Method and Theory*, 24(3):703–725, 2017. 1

[67] Jingyi Yu, Leonard McMillan, and Steven Gortler. Surface camera (scam) light field rendering. *International Journal of Image and Graphics*, 4(04):605–625, 2004. 2

[68] Mingjie Zhang, Xing Lin, Mohit Gupta, Jinli Suo, and Qionghai Dai. Recovering scene geometry under wavy fluid via distortion and defocus analysis. In *European Conference on Computer Vision (ECCV)*, 2014. 2

[69] Qi Zhang, Chunping Zhang, Jinbo Ling, Qing Wang, and Jingyi Yu. A generic multi-projection-center model and calibration method for light field cameras. *IEEE Transactions on Pattern Analysis and Machine Intelligence*, 41(11):2539–2552, 2018. 2, 6, 7